High contrast imaging and flexible photomanipulation for quantitative *in vivo* multiphoton imaging with polygon scanning microscope

Y X Li[1], S J. Montague[1,2], A Brüstle[3], X F He[1], C Gillespie[4], K Gaus [5, 6], E E. Gardiner[2], W M Lee[1,2,7*]

[1] *Research School of Engineering, College of Engineering and Computer Science, The Australian National University, 31 North Road, Canberra, ACT, Australia 2601*
[2] *ACRF Department of Cancer Biology and Therapeutics, The John Curtin School of Medical Research, The Australian National University, 131 Garran Road, Canberra, ACT, Australia 2601*
[3] *Department of Immunology and Infectious Disease, The John Curtin School of Medical Research, The Australian National University, 131 Garran Road, Canberra, ACT, Australia 2601*
[4] *Imaging and Cytometry Facility, The John Curtin School of Medical Research, The Australian National University, 131 Garran Road, Canberra, ACT, Australia 2601*
[5] *Australia- EMBL Node in Single Molecule Science, School of Medical Sciences, University of New South Wales, Sydney NSW 2052 Australia*
[6] *Australia Research Council Centre of Excellence in Advanced Molecular Imaging, University of New South Wales, Australia*
[7] *The ARC Centre of Excellence in Advanced Molecular Imaging, The Australian National University, ACT 2601 Australia*
[†] *Corresponding author: steve.lee@anu.edu.au*

Abstract: In this paper, we introduce two key improvements that overcome limitations of existing polygon scanning microscopes whilst maintaining high spatial and temporal imaging resolution over large fields of view (FOV). First, we proposed a simple and straightforward means to control the scanning angle of the polygon mirror to carry out photomanipulation without resorting to high speed optical modulators. Second, we devised a flexible data sampling method directly leading to higher image contrast by over 2 folds and digital images with 100 megapixels (10240 x 10240) per frame at 0.25 Hz. This generates sub-diffraction limited pixels (60 nm per pixels over the FOV of 512 µm) which increases the degrees of freedom to extract signals computationally. The unique combined optical and digital control recorded fine fluorescence recovery after localized photobleaching (r ~10 µm) within fluorescent giant unilamellar vesicles (GUVs) and micro-vascular dynamics after laser induced injury during thrombus formation *in vivo*. These new improvements expand the quantitative biological-imaging capacity of any polygon scanning microscope system.

Keywords: Scanning microscopy; Optical design and fabrication; Multiphoton Microscopy

Introduction

Multiphoton laser scanning microscopes selectively excite fluorophores only close to the focus, based on multiphoton absorption [1]. Since laser scanning microscopes use a concentrated stream of focused light on the sample, they can be used to localize high energy laser exposure at sub-micrometer accuracy on the sample [2]. Local photo-manipulation using laser scanning microscopes facilitate a straightforward means to control and visualize photoconversion [3], vascular permeability [4], focal brain injury [5] and microinfarcts [6]. Photo-manipulation based vascular injury models provide avenues to investigate microvascular injury in specific microenvironments [7, 8] and to observe the influence of complex fluid dynamics behind platelet deposition and coagulation.

In optical digital imaging, it is highly desirable to ensure that different imaging parameters are satisfied including space product bandwidth (SBP) and signal to noise ratio (SNR). In digital optical imaging, space bandwidth product (SBP) defines the density of pixel over a given field of view [9]. SBP is simply the calculation of total number of imaging points (pixels) within the field of view (FOV). In an ideal optical imaging setup, the size of each image pixel is assumed to match the optical diffraction limit spot. This meant that the optical resolution (point spread function) is adequately sampled by a set of pixels over the entire FOV. By fulfilling SBP, it is then possible to record biological events in a single snapshot that may otherwise be missed. Also, it has been shown that localization super-

resolution microscopy techniques using imaging photo switchable fluorophores through computational processes can only be achieved from pixel sizes that are much smaller than the diffraction-limited spot [10]. On the other hand, signal to noise ratio in laser scanning fluorescence imaging system is dependent on laser dwell time, quantum efficiency of fluorophores, laser repetition rate and background noises (i.e. optical scattering and electronics).

For camera-based systems, the pixel density is fixed by the number of photodetectors that are spatially separated on the camera and the imaging contrast depends on the sensitivity of each detector. Laser scanning microscopes use a single large area detector (photomultiplier tube, PMT or avalanche photodiode, APD) to collect a stream of fluorescence photons excited by a single excitation point. As such, the position where the spatial location of the fluorescence emitted is encoded via the pixel clock. Unlike a camera system, which uses an array of photodetectors that maps the fluorescence photons onto separate spatial positions on the sample, laser scanning microscopes allocate pixels to a single fluorescence emission point based on read out rate of the imaging system (i.e. pixel clock). For a fixed laser dwell time, a faster pixel clock meant that the single detector is repeatedly collecting the emitted fluorescence signals. The increase of pixels allocated to a diffraction limited spot is likely to result in an increase in signal, akin to frame averaging. Hence, tailoring the pixel clock can increase both image contrast and add a higher density of pixels to the image. In laser scanning microscopy, the increase of pixel density over the same FOV leads to higher SBP and SNR. Overall, the technical challenge for a system to achieve a high speed raster

scanning, and high SBP over the full FOV is to tailor dynamic feedback control over the data sampling parameters (pixel clock, scanning rate).

Combining photomanipulation, high SBP and video rate imaging in mirror scanners

Mirror-based scanners [11-13] are well suited for multiphoton microscopy because it possesses high optical reflectivity and low optical dispersion. Although conventional galvanometer mirrors alone can achieve both imaging and photomanipulation, the high rotational inertia of galvanometer mirror scanners limits its line scanning speed from achieving video rate speed of imaging. Also, most mirror-based laser scanning microscopes produce a SBP ~0.2 to 0.4 megapixels with a fixed pixel clock. Typically for microscope objective lens of NA = 1 and FOV = 500 μm with 500 nm diffraction limit, the corresponding SBP is approximately 1 megapixels. For a laser scanning system to record fine spatially fluctuating fluorescence with limited SBP [12, 13], one needs to narrow the laser scanning field as shown in Figure 1a) to construct a smaller imaging field of view (FOV) as shown in Figure 1b) i) to increase sampling ratio. This fills up only a fraction of the full imaging field of view that in turns lowers the imaging throughput of a microscope as depicted in Figure 1b) ii). If the SBP can be increased over a larger field of view, it would be possible to capture the full imaging field and record all the biological events. This will directly increase accuracy in fine spatial fluorescence signal quantification at high spatial and temporal resolution.

Many laser scanning microscopy systems often resort to the combination of two separate scanning systems to achieve both photomanipulation and video rate imaging. Video imaging is supported by mirror scanners that operate through resonant scanning or spinning multi-

facet polygon mirrors. These scanners can achieve line scanning rates of 8 kHz or greater. The scanning angle of resonant mirrors can be narrowed to achieve photomanipulation, but it possesses a non-uniform scanning velocity pattern which creates undesirable dwell time at the edges of a scan field [14].

Amongst the laser scanning technologies, the polygon mirror scanner has proven to deliver high linearity and high scanning speeds over an entire imaging field and generates imaging speed of up to 60 Hz [11] or even 200 Hz [15] *in vivo*. However, polygon mirrors face the limitations of a fixed scanning angle and cannot perform photomanipulation. High speed light modulators (acousto-optics or electro-optics [16]) could be used to selectively pattern the scanning intensity, but they accrue additional losses in optical energy, either through optical polarization, diffraction or increased optical aberrations [17]. Alternative approaches such as random access scanning [18], temporal focusing methods [19] and collinear aligning of a second photomanipulation beam offer greater flexibility, but they are also constrained by lower optical efficiency due to diffraction and chromatic aberrations leading to a reduction of axial resolution [20, 21]. Additional conjugate scanning devices [22] are required to construct the second photomanipulation beam path which demands additional optical power. What is lacking is a flexible, straightforward and efficient means of achieving localized photomanipulation in a video rate polygon mirror imaging system. In summary, a straightforward modification of video rate laser scanning microscope that can deliver a combination of localized photomanipulation, tunable imaging speeds greater than 5 - 25 Hz at high SBP (1920 x 1080) over the full FOV, can accurately interrogate specific biological events at cellular level *in vivo* [23, 24]. High resolution spatial-temporal quantitative

molecular measurements using multiphoton microscopes include fluorescence recovery after photobleaching (FRAP), where fluorescence signals are tracked before and after a photobleaching event to estimate the diffusion coefficient of fluorescence molecules [25]. Another imaging measurement is the monitoring of real time vasculature parameters after laser-induced injury, with parameters of interest including thrombus size and volume. Other vascular parameters (leaking, blood flow rates) are further indicators of platelet function at the thrombus–vessel wall interface *in vivo* [26].

Here, we propose direct and straightforward modifications to a video rate polygon scanning microscope system to achieve high contrast imaging and localized photo-manipulation with variable SBP imaging controls. With this new configuration, we are able to achieve localized photo-manipulation during imaging. The flexible data sampling method is enabled by manipulating the rotation rate of the polygon mirror and the sampling rate of the acquisition system. We demonstrate that the flexible sampling method that yields SBP of 100 megapixels as well as doubling image contrast. Since the new system can produce sub-diffraction limited pixel size of 60 nm at imaging speed of around 5 Hz, it fulfils the conditions necessary to implement super-resolution localization microscopy methods [10].

In the following sections, we described in detail how the FOV is segmented and then reassigned over the imaging field. We further illustrate how high pixel density images are acquired by synchronizing the polygon rotation rate along with the image acquisition. Finally, we demonstrate the capability of the new system by conducting quantitative photo-manipulation experiments using FRAP and real-time visualization of microvascular dynamics during laser induced micro-occlusion in living mice.

Results

Amplitude based segmented FOV reassignment in polygon mirror

Carlson and colleagues [27] made use of a simple amplitude mask placed at the image plane of a video-rate, polygon mirror scanning system to restrict intensity on individual photoconvertible cells to convert their fluorescence signal. This method retains high speed imaging but does not offer sufficient flexibility for arbitrary patterning. Whilst a programmable, diffractive, liquid crystal display can assist in tailoring the intensity pattern, it would incur high intensity losses and require polarization controls.

The main principle behind the new configuration is that a small segment of the scanning field at the image plane is selected with an amplitude mask e.g. binary slit or liquid crystal modulator. The segmented scan field is then shifted along the image plane by a second galvanometer. The mask is allocated onto the image conjugate plane, which provides the additional benefits of capturing the real-time event of the localized area caused by the photomanipulation process as it happens in real-time. We named this two-step process as FOV reassignment. The first stage was to select a small scanning field at the focus of the lens (L1) after the polygon mirror (PM) using a binary slit. The slit (S1) is much larger (> 20 x) than the diameter of the beam spot at the focal plane. As depicted from a view along the beam propagation direction in Figure 2 a) ii), the slit is placed at the focal plane to select a small scanning line. In the second stage, the segmented line scan is projected onto a pair of galvanometer mirrors, GM1 and GM2 which are positioned on the conjugate plane of the polygon mirror (PM) after second relay lens (L2). GM1 and GM2 provide a horizontal beam translation (x-axis) and a vertical beam translation (y-axis) respectively. Both GM1 and PM mirror share the same beam translation axis. This means the introduction of a tilt ($_{,1}$) on

GM1 would shift the segmented line intensity along the x-axis and, at the same time, a tilt on GM2 would shift the beam along the y axis as shown in Figure 2 a) iii). The segmented scan line is expanded into large scan area (square intensity pattern) by continuously changing the scanning angle of GM2 as shown in Figure 2 a) iv). By controlling the tilt angle of GM1 and GM2, a square shaped scanning intensity pattern can be repositioned along the sample plane to achieve localized photomanipulation as shown in Figure 2 a) iv). We chose a square intensity pattern by setting the galvanometer mirror voltages to ensure symmetrical intensity distribution for photomanipulation. In the setup, we used a slit (Thorlabs: S150R) with a width of 150 μm as our mask, to segment a portion of the scanning line. Based on the magnification factor of the optical system, a 150 μm binary slit provides an approximate projected intensity area of around 14.4 μm width. In order to toggle between localized photobleaching and large FOV imaging, we employed a mechanical flip to switch between two elements: a binary slit and a half wave plate. It is possible to swap the slit with masks of different patterns to obtain less symmetrical intensity patterns. The half wave plate, together with a second polarization beam splitter (not shown in the diagram), was used to reduce the overall intensity of the beam for imaging purposes. The width of the slit is larger than the beam by ~ 10 folds which does not reduce the intensity of the single laser beam passing through the slit. Since the beam is scanning continuously, the slit effectively transmits intensity at a certain percentage of the time. For a given scan rate, the duty cycle (ratio between the scanning line over the slit size) determines the optical power after the slit. For a 150 μm slit, the duty cycle of the illumination is reduced to around 6%.

To demonstrate the flexibility of the system to achieve photomanipulation, Figure 2 b) shows the experimental results before and after multiple, localized photobleaching events of sites on auto-fluorescent pollen grains. Figure 2 b) i) shows an image of a fluorescent pollen grain (20 fps, averaged 1 s) chosen for the experiment. We then preselected several positions to sequentially conduct photobleaching as shown in Figure 2 b) ii). Since photobleaching of the area is achieved through laser scanning, rather than through a single stationary focus spot, we anticipated some level of non-uniform bleaching. This means that the photobleached area could be larger than the anticipated illumination due to spatial bleed-through. As such, it is necessary to verify the minimum accuracy of the photobleaching area by measuring the non-photobleached region between two adjacent photobleached sites. Based on the position that we selected to photobleach, we chose two adjacent sites where the bleaching area could be individually resolved as shown in Figure 2b) ii) (white dotted box). Figure. 2b) iii) shows the cross-sectional fluorescence signals between the two adjacent sites. Compared with the rest of the photobleached sites from Figure. 2b) ii), we found that the average separation between two closely photobleached sites of 14 μm, was around 2.4 μm. This defined the minimum spatial interval of the photomanipulation site, representing the closest distance between the two chosen photomanipulation sites that could be achieved.

Dynamic scanning and sampling control

Here we show how imaging contrast and SBP of a laser-scanning microscope can be controlled by dynamically manipulating the scanning speed of the beam, sampling rate of the photon detector and data acquisition rate. Figure 3 a) shows how the line scan rate (L) of a polygon mirror is measured by a photodiode and injected into the frame grabber card to

determine the frame rate of the imaging system via vertical synchronisation (VSync). Equation (1) shows the interdependence of the line rate and the sampling rate.

The sampling rate of the system (S) is equivalent to the product of the total number of pixels in a single frame ($H_{pixel} * V_{pixel}$) as described by the following equation:

$$S = H_{pixel} * \ V_{pixel} * \left(\frac{L}{V_{pixel}}\right) \quad (1)$$

in which the referencing pixel amount is 512 x 512. The frame rate described in equation (1) is simply the division of the line scan rate (L) (also known as Hsync) by the number of pixels in the vertical direction (V_{pixel}).

Figure 3 shows that the reduction of pixel dwell time at different line scan rate from 10.8 kHz in Figure 3(b) and 3(c) to 5.4 kHz in Figure 3(d) and the corresponding reduction in frame rate from 20 fps to 10 fps. By tuning the pixel sampling rate with different line rates, it is possible to increase both the SNR and SBP parameters simultaneously. Figure 3b) and Figure 3c) have the same line scan rate of 10.8 kHz but different pixel sampling rate of 10 MHz and 30 MHz. While Figure 3d) is taken with the same pixel sampling rates of 30 MHz as Figure 3b) but slower line scan rate of 5.4 kHz . With higher sampling rates, SBP is increased by 10-fold which means that the pixel size changes from 1.2 µm to 120 nm. The inset of Figure 3 b) - c) shows how individual 3 µm fluorescent microspheres are resolved with much higher SBP. We quantify the contrast improvement by fitting the intensity distribution of the fluorescence microspheres to Gaussian curves as shown in Figure 3 e) to g). The measured averaged diameter of the spheres are 3 ± 0.2 µm and the image contrast (I_{max}-I_{min})/(I_{max}+I_{min}) also improves from 32% to 67% by fitting the beads diameter. For the images

shown in Figure 3, the vertical axes were fixed at 512 pixels. By increasing the pixel clock and slowing the line rate (5.4 kHz) as shown in Figure 3d), we allocate and collect more photons onto a given spatial position where the beam is positioned. This results in an increase in signal and avoids the need to time averaging each image. However, this led to a reduction of the imaging frame rate from 20 Hz to 10 Hz as more pixels are generated. An even higher SBP can be achieved by reducing scanning line speed to 5 kHz and frame rate reduces to 5 Hz.

Aside from tuning the sampling rate, the contrast of the multiphoton polygon mirror system is fundamentally limited by repetition rate of the pulsed laser, sampling rate of the imaging system and quantum efficiency of the PMT versus the stochastic process behind fluorescence signal background noise. The repetition rate of the pulsed laser corresponds to the number of photon incident onto the sample. Based on the repetition rate of our laser which was 82 MHz, the reduction of the line scan rate from 27 kHz to 2.7 kHz increased laser pulses from 3037 to 30370 pulses. For quantum efficiency of the photodetector is given by $\frac{\lambda^2}{\bar{N}\sigma^2}$ where λ and σ are the mean and standard deviation of the fluorescence signal in the pixel sampling interval, $\bar{N}$ is the mean number of the photons collected within a given pixel sampling interval [28]. The width of the pulse signal about 100 ns based on the rise time of PMT (Hamamatsu: R928) and PMT amplifier (Hamamatsu: C9999). Therefore, the maximum sampling rate is 20 MHz at least for capturing each pulse from the PMT. In order to achieve the ideal efficiency of 1, the change in the number of photons would alter the efficiency of photodetector. In summary, either an increase in the sampling rate or reduction in the line scan rate provided an increase in photons collected per pixel over a given interval and enhanced the signal to noise ratio.

Next, we looked for the optimal configuration that combines video rate imaging and high SBP. As it turns out, the maximum possible SBP for a 36 facets polygon mirror, which can operate at 30 Hz, is around 2 megapixels over a FOV of 512 x 512 μm^2. The SBP achieved here is an order of magnitude higher than any existing laser mirror scanning microscopes. High SBP images with sub-diffraction limited pixel size have played a key role in improving images beyond the diffraction limit [10, 29]. This also benefits quantitative, fluorescence measurements such as FRAP [30], deconvolution [14] and localized microscopy [10].

In Figure 4, we attained the maximum SBP of 100 megapixels with lowest pixel dwell time by reducing the laser scanning line from 21.6 kHz to 2.7 kHz and increasing the sampling rate from 20 MHz to 30 MHz. This results in an imaging frame rate of 5 fps. Figures 4 a) and b) compare the images of a slice of fixed human kidney tissue that was taken over the full FOV with a SBP of 0.2 megapixels and a time-averaged over 2 seconds and SBP of 100 megapixels over 4 seconds. The full image with SBP of 100 megapixels is achieved by stitching 20 images of 5 megapixels each (10240 x 512). Both images shown in Figure 4 a) and b), have undergone blind deconvolution. To quantify the achievable resolution with high SBP, we imaged sub-diffraction limited spheres with 0.175 μm diameter (PS-Speck, P7220). Figure 4 c) and d) show two closely-spaced spheres before and after blind deconvolution respectively. Figure 4 e) shows the line-plots of the fluorescence intensity across the spheres and their respective Gaussian fit, where the deconvolution image is able to resolve two spheres separated by ~ 1 μm. We note that 0.175 μm only appears as a single pixel for conventional 512 x 512 pixels resolution and cannot be deconvoluted at all. Instead, Figures 4

c) and d) show that a higher SBP can lead to positive imaging enhancement through deconvolution. To this end, we showed that a high SBP greatly improves both the imaging contrast and enhances computational approaches to improve image quality.

PScan 1.1

Previously, we described a new software framework around the polygon mirror microscope [11] and incorporated these new functions into the PScan software framework [11]. Figure 5 a) shows an image of the user interface for PScan1.1 that includes new options such as blind deconvolution, averaging (red square), targeting photomanipulation (blue square) and flexible pixel sizes (orange square). The photomanipulation function allows input coordinates (green cross cursor) into the program. Deflection voltage with distance needs to be calibrated prior to image acquisition. The effective multi-site scanning period can be 200 s long. In Figure 5, we show a cropped image of a pollen grain taken at 1.2 μm pixel size with four pre-selected positions before (Figure 5 b)) and after (Figure 5 c)) photobleaching. This is followed by a high SBP image captured in real time to achieve a digitally magnified image as shown in Figure 5 d). We have embedded all these functions into PScan to enable seamless control over automated photomanipulation, high speed imaging and oversampling.

Multi-site FRAP

The combination of high SBP imaging and photomanipulation is useful for techniques such as FRAP and laser-induced thrombosis. FRAP techniques work by first targeting a localized site for photobleaching, followed by monitoring of recovery of the fluorescence signal. The time for recovery of fluorescence reflects diffusion dynamics of fluorescence molecules

within the medium of interest (water or lipid). For aqueous solution, we use fluorescein isothiocyanate (FITC) dissolved in water and for lipid media, we generated sulforhodamine B-labelled giant unilamellar vesicles (GUV) using electroformation techniques [31].

We first conducted a single site photobleaching in a FITC solution and measured the time it takes for the fluorescence signal to recover. Figure 6 a) i) shows the full view of the sample just after photobleaching occurred (red box). Figure 6 a) ii) is a cropped and digitally magnified version of the same image. With a pixel size of 1.2 µm and low SBP (0.2 megapixels), the fluorescence signal recorded shows high pixelated. Figure 6 a) iii) to v) show the increase in pixel size by factor 10 (120 nm) with a SBP of 2 megapixels, we observed sequential recovery of the fluorescence signal at 0, 1 and 22 seconds. The average fluorescence recovery in the higher SBP image (white circle) over time (shown in Figure 6 b)) displayed the typical exponential recovery rate. Comparing Figure 6 a) ii) and iii), small changes in fluorescence intensity, that were not detectable at low pixel counts, are now readily observed. The exponential fit, $I_0(1-e^{-\gamma t})$, shown in Figure 6 b), retrieved the recovery time (γ). The recovery time γ is 0.7845 s and fluorescence intensity I_0 is 0.7572, which gives a diffusion coefficient of 8.96 µm^2/s that compares well with previous studies [30]. Next, we conducted FRAP measurements using sulforhodamine B-labelled GUVs. The GUV is made with 2.5 µM sulforhodamine B labelled sucrose through the process of electroformation [31]. Instead of single site photobleaching, we selected two separate sites and monitored the recovery of diffusing fluorescence material. The fluorescence recovery rate in GUVs was retrieved using a modified fitting equation $I_0(a-e^{-\gamma t})$ with *a* representing residual fluorescence after bleaching. Based on the fitted parameters (first site: I_0 = 0.1417, *a*

= 7.0836, γ = 0.2427 and second site: I_0 = 0.1231, a = 8.1612, γ = 0.3543), the diffusion coefficient is given by 3.71 $\mu m^2/s$ and 5.40 $\mu m^2/s$ respectively. The discrepancy between the coefficients can be attributed to the different amount of photobleaching achieved. Based on the time trace in Figure 6, we can see that the level of fluorescence after photobleaching is higher at one site over the other, which could result in the difference in the measured diffusion coefficients as less molecules are need to be replenished, which is consistent with previously published FRAP measurements using a galvanometer mirror scanner [30].

Multiphoton-mediated *in vivo* vascular laser injury

A laser-induced vascular injury aims to remove the endothelial cells lining a blood vessel and expose the subendothelial matrix (containing thrombotic collagen and von Willebrand factor) to blood constituents. This technique enables the precise activation of a local coagulopathy within a flowing vasculature, without causing excessive bleeding (plasma extravasation or hemorrhage). Here we first aimed to induce a precise laser-mediated injury using the reassignment method and then increase the SBP of the image at real time, to achieve smaller pixel sizes and quantify onset and progression of thrombus formation within the microvasculature. We chose a site close to the femoral vein of an anaesthetized mouse. We injected tetramethyl rhodamine isothiocyanate (TRITC)-dextran to visualize blood flow within the vasculature and monitor vascular dynamics [32].

Figure 7 a) and b) show still images of fluorescently-labelled blood flowing through a vessel before and after the laser induced injury, with pixel sampling of 170 nm (SBP of 2 megapixels) at a frame rate of 20 Hz respectively. Figure 7 c) is a schematic, depicting the site of induced injury and bleeding sites within the vessel. We also tracked the corresponding

flow dynamics along the main vasculature (insert dotted white line) over time. We then plotted a line scan along the flowing vessel against time in Figure 7 d) which allows us to monitor the evolution of the micro-embolization dynamics. Figure 7 d) shows that a thrombotic occlusion occurred around t=30 s and first expanding in size along the flow until time t=60 s before collapsing (embolizing) at t=125 s. Without any additional laser injury, we observed that the site reached a second wave of embolization at t=128 s. During this time point, there are also several local sites of haemorrhage evident as indicated by fluorescently stained blood leaking at positions i) and ii). We also plotted the leaking with a line plot of the fluorescence signal over time as shown in Figure 7 e). Aside from the leaking of vascular contents, we also observed considerable fluid accumulation along the main (iii), (iv) and adjacent vasculature (v). Figure 7 f) summarizes the changes in fluorescence intensity over time at points (iii) to (v). We can see a sudden build-up of fluid at t=155 s with an increase in fluorescence, which can be attributed to the second embolization event occurring earlier (at t=128 s). The images and time course of thrombus formation are consistent with activated platelets adhering to exposed collagen at a site of vessel injury and recruiting new platelets, which are bridged by fibrinogen. Fibrin results from the local generation of thrombin, facilitated by activated platelets. Thrombin cleaves fibrinogen to form fibrin, which polymerizes into a fibrous gel to stabilize a thrombus and seal the injured blood vessel [26].

Conclusion

Until now, the polygon mirror scanning microscope system was useful in high speed imaging systems but did not provide any form of photomanipulation capabilities or SBP greater than

0.4 megapixels. Here, we demonstrate the utility of a polygon mirror system for FRAP or laser-induced thrombosis studies by simply inserting a binary slit and a second galvanometer mirror. We have greatly enhanced the functionality of existing polygon scanning rates to permit the changing of the SBP (0.2 to 100 megapixels) where pixel size reduces from 1.2 µm down to 60 nm over an entire scanning field and the corresponding imaging contrast increases by 2 folds. The imaging SBP being achieved here is an order of magnitude higher than existing laser scanning microscopes. There are, however, limitations in our current system. Firstly, the switching rate between imaging and photomanipulation is limited by the rotation rate of the mechanical flipping mount (stepper motor) of 2 Hz. Secondly, the lower optical power exiting the aperture needs to be improved. Lastly, the current setup uses a fixed mask which has a finite photomanipulation area. The limitations of the mechanical flip mount can be overcome by using a motor with less inertia or higher torque. This will result in reducing the flipping action to around tens of milliseconds (e.g. Zaber: X-FWR-E have switching time of 57 ms). The lowering of total sample illumination power by the localized slit is compensated easily by increasing the laser pump power. The fixed mask can be swapped with an adjustable pinhole. . In conclusion, the new polygon microscope displays the highest SBP at video rate that when combined with photomanipulation capabilities can achieve a greater breadth of quantitative in vivo imaging that was not possible before in polygon scanning mirrors. Furthermore, this method can also open up multi-FOV adaptive optics corrections [33] or localized super-resolution microscopy[10].

Methods

Microscope

The system is based on a multiphoton microscope that integrated a pair of orthogonal galvanometer scanning mirrors (Cambridge Technology: 6220H, 7 mm x 5 mm) and a polygon scanner (Lincoln Laser: DT-36-250-025, 4.8 mm x 5.0 mm) that provided raster scanning. All the scanning mirrors were tele-centrically conjugated to each other and shared a common pupil with the objective back aperture. The imaging laser was a Ti-Sapphire pulse laser (Tsunami, Spectra Physics) that was tuneable from 680-920 nm with a repetition rate of 82 MHz and approximately 100 femtoseconds pulse-width at maximum 800 mW output power. The optical power was tuned using a half wave plate (HWP) with a polarization beam splitter (PBS). The beam after the HWP was first expanded by 4 times to fill the aperture of the scanning mirrors before relaying onto the back aperture of the microscope objective (MO) using 3 conjugate lens pairs. We chose an objective lens (Zeiss: 20x, 1.00NA/water) with a long working distance of 3.5 mm, suitable for deep tissue imaging. Based on the chosen tube lens (L10, 100 mm), the effective imaging magnification was around 10x and laser power around 20 - 30 mW after the objective for imaging. The excitation wavelength was manually tuned and monitored with a Czerny-Turner spectrometer (CCS175/M, Thorlabs) placed close to the output of the laser. The emitted fluorescence signal was separated from the excitation light by a dichroic long-pass filter (Semrock, FF665-Di02). The emitted fluorescence was then split again by a standard dichroic filter (FF562-Di03-25x36) into green and red fluorescence, then further filtered with emission filter (Semrock: FF01-593/40, FF01-543/22-25). The individual fluorescence signals were collected by two photomultiplier tubes and displayed as red and green channels respectively.

GUVs and Fluorescein

FITC solution was made by thoroughly mixing 10 mM FITC powder in phosphate-buffered saline, pH 7. GUVs were made by mixing diphytanoyl phosphatidylcholine DPHPC (Avanti Polar Lipids) encapsulating 2.5 μM sulforhodamine B (Sigma-Aldrich) in 100 mM sucrose solution, through an electro-swelling device for 200 minutes (Nanion: Vesicle Prep Pro). GUVs were then diluted in 100 mM glucose solution.

Mice preparation for *in vivo* imaging

Prior to imaging, all mice were housed in cages with free access to food and water, temperature/humidity control, ventilation, and regular cleaning. All animal experiments were performed using procedures approved by the Australian National University Standing Committee for Ethical Research Using Animals (protocol 2016/46). C57BL/6 mice were injected with rhodamine-labelled dextran (70 kDa) at 20% wt and 20 μl was injected retro-orbitally. For anesthesia, a ketamine/xylazine solution was freshly made by mixing 1 ml of ketamine (100 mg/ml), 0.15 ml of xylazine (100 mg/ml) and 8 ml of sterile saline under aseptic conditions and used on the same day. The anaesthetized mouse was placed on a heated stage (37^{o}C) and the femoral vessel exposed for imaging.

Acknowledgements

We thank M. Castanares, Y. Wang, I. Cockburn, M. White and V. Daria for experiment assistance. We are grateful for additional funding support from William Heath. We also recognize B. Condon for making the trigger amplifier electronic circuit. We thank C. Alt (MGH), A. Upadhya, Thomas Mcmenamin and T. Kamal for detailed proof reading of the manuscript.

Contributions

W. M. Lee conceived and supervised the project. W. M. Lee and Y. Li designed and constructed the optical system. Y. Li developed the control system, wrote the PScan software and processed and analyzed all the experimental data. Y. Li, W. M. Lee and S. Montague performed the *in vivo* experiments with support from E. Gardiner, C. Gillespie, K. Gaus, A. Bruestle and C. Gillespie. X. He assisted with fluorescence beads and GUVs fabrication respectively. All authors participated in discussions and data interpretation. Y. Li and W. M. Lee wrote the paper with input from all authors.

References

1. Webb, R.H., *Confocal optical microscopy.* Rep. Prog. Phys., 1996. **59**: p. 427-471.
2. Avula, U.M.R., et al., *Cell-selective arrhythmia ablation for photomodulation of heart rhythm.* Science Translational Medicine, 2015. **7**(311): p. 311ra172-311ra172.
3. Chtanova, T., et al., *Real-time interactive two-photon photoconversion of recirculating lymphocytes for discontinuous cell tracking in live adult mice.* Journal of Biophotonics, 2014. **7**(6): p. 425-433.
4. Choi, M., et al., *Minimally invasive molecular delivery into the brain using optical modulation of vascular permeability.* Proceedings of the National Academy of Sciences, 2011. **108**(22): p. 9256-9261.
5. Davalos, D., et al., *ATP mediates rapid microglial response to local brain injury in vivo.* Nature Neuroscience, 2005. **8**(6): p. 752-758.
6. Shih, A.Y., et al., *The smallest stroke: occlusion of one penetrating vessel leads to infarction and a cognitive deficit.* Nature Neuroscience, 2013. **16**(1): p. 55-63.
7. Furie, B. and B.C. Furie, *Thrombus formation in vivo.* Journal of Clinical Investigation, 2005. **115**(12): p. 3355-3362.
8. Ivanciu, L., et al., *A zymogen-like factor Xa variant corrects the coagulation defect in hemophilia.* Nature Biotechnology, 2011. **29**(11): p. 1028-1033.
9. Zheng, G., R. Horstmeyer, and C. Yang, *Wide-field, high-resolution Fourier ptychographic microscopy.* Nature Photonics, 2013. **7**(9): p. 739-745.
10. Dertinger, T., et al., *Fast, background-free, 3D super-resolution optical fluctuation imaging (SOFI).* Proceedings of the National Academy of Sciences, 2009. **106**(52): p. 22287-22292.
11. Li, Y., et al., *Flexible polygon-mirror based laser scanning microscope platform for multiphoton in-vivo imaging.* Journal of Biophotonics, 2017. **1**(10.1002/jbio.201600289).

12. Stirman, J.N., et al., *Wide field-of-view, multi-region, two-photon imaging of neuronal activity in the mammalian brain.* Nature Biotechnology, 2016. **34**(8): p. 857-862.
13. Sofroniew, N.J., et al., *A large field of view two-photon mesoscope with subcellular resolution for in vivo imaging.* eLife, 2016. **5**: p. e14472.
14. Callamaras, N. and I. Parker, *Construction of a confocal microscope for real-time x-y and x-z imaging.* Cell Calcium, 1999. **26**(6): p. 271-279.
15. Choi, S., et al., *Development of a high speed laser scanning confocal microscope with an acquisition rate up to 200 frames per second.* Optics Express, 2013. **21**(20): p. 23611-23618.
16. Urban, B.E., et al., *Super-resolution two-photon microscopy via scanning patterned illumination.* Physical Review E, 2015. **91**(4): p. 042703.
17. Römer, G.R.B.E. and P. Bechtold, *Electro-optic and Acousto-optic Laser Beam Scanners.* Physics Procedia, 2014. **56**: p. 29-39.
18. Katona, G., et al., *Fast two-photon in vivo imaging with three-dimensional random-access scanning in large tissue volumes.* Nature Methods, 2012. **9**(2): p. 201-208.
19. Oron, D., E. Tal, and Y. Silberberg, *Scanningless depth-resolved microscopy.* Optics Express, 2005. **13**(5): p. 1468-1476.
20. Lechleiter, J.D., D.-T. Lin, and I. Sieneart, *Multi-Photon Laser Scanning Microscopy Using an Acoustic Optical Deflector.* Biophysical Journal, 2002. **83**(4): p. 2292-2299.
21. Kirkby, P.A., K.M.N. Srinivas Nadella, and R.A. Silver, *A compact acousto-optic lens for 2D and 3D femtosecond based 2-photon microscopy.* Optics Express, 2010. **18**(13): p. 13720-13744.
22. Go, M.A., et al., *Targeted pruning of a neuron's dendritic tree via femtosecond laser dendrotomy.* Scientific Reports, 2016. **6**: p. 19078.
23. Fritzsche, M. and G. Charras, *Dissecting protein reaction dynamics in living cells by fluorescence recovery after photobleaching.* Nature Protocols, 2015. **10**(5): p. 660-680.
24. Kochen, J.A. and S. Baez, *Laser-induced microvascular thrombosis, embolization, and recanalization in the rat.* Annals of the New York Academy of Sciences, 1965. **122**(1): p. 728-737.
25. Sullivan, K.D., A.K. Majewska, and E.B. Brown, *Single and Multiphoton Fluorescence Recovery after Photobleaching.* Cold Spring Harbor protocols, 2015. **2015**(1): p. pdb.top083519-pdb.top083519.
26. Dubois, C., et al., *Thrombin-initiated platelet activation in vivo is vWF independent during thrombus formation in a laser injury model.* Journal of Clinical Investigation, 2007. **117**(4): p. 953-960.
27. Carlson, A.L., et al., *Tracking Single Cells in Live Animals Using a Photoconvertible Near-Infrared Cell Membrane Label.* PLOS ONE, 2013. **8**(8): p. e69257.
28. Pologruto, T.A., B.L. Sabatini, and K. Svoboda, *ScanImage: Flexible software for operating laser scanning microscopes.* BioMedical Engineering OnLine, 2003. **2**(1): p. 13.
29. Bechhoefer, J., *What is superresolution microscopy?* American Journal of Physics, 2015. **83**(1): p. 22-29.

30. Deschout, H., et al., *Straightforward FRAP for quantitative diffusion measurements with a laser scanning microscope.* Optics Express, 2010. **18**(22): p. 22886-22905.
31. Méléard, P., L.A. Bagatolli, and T. Pott, *Giant Unilamellar Vesicle Electroformation.* Methods in Enzymology, 2009. **465**: p. 161-176.
32. Pink, D.B.S., et al., *Real-Time Visualization and Quantitation of Vascular Permeability In Vivo: Implications for Drug Delivery.* PLOS ONE, 2012. **7**(3): p. e33760.
33. Park, J.-H., et al., *Large-field-of-view imaging by multi-pupil adaptive optics.* Nature Methods, 2017. **14**(6): p. 581-583.

Figure 1

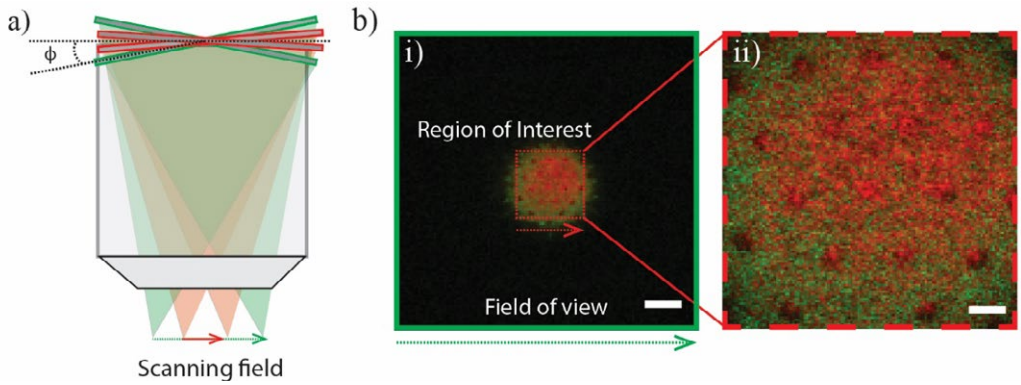

Figure 1: Changing the scanning field and field of view (FOV)
a) Schematic depicting a scanning field changing at the focus of a microscope objective. b) Image of fluorescently-tagged pollen displayed after digitization i) shows the full field of

view (FOV) of a pollen sample (Scale bar 20 μm) ii) magnified image after reducing the scanning field onto the region of interest (Scale bar 5 μm) .

Figure 2

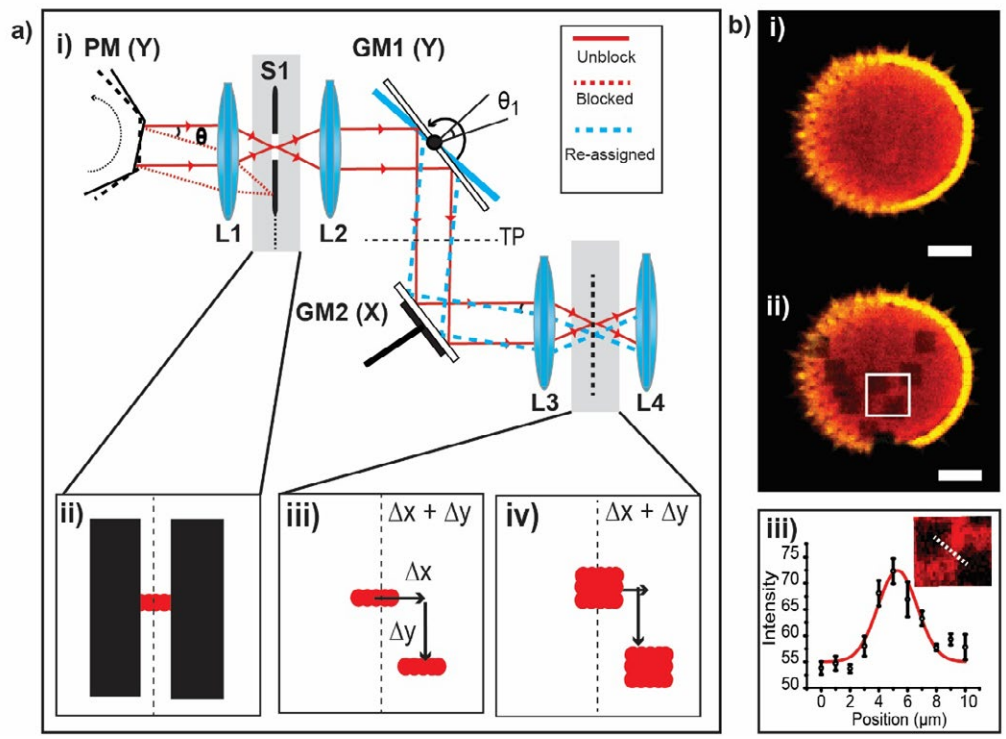

Figure 2: Amplitude based FOV control in polygon mirror scanning

a) Schematic of amplitude based FOV control to achieve localized photomanipulation. i) Schematic illustration of how a single slit is used to segment a small scan area and relocated along the sample to achieve localized photomanipulation. PM (Y): polygon mirror for y-axis scanning- fast axis, S1: flip flopper slit, TP: telecentric plane, GM1 (Y) and GM2 (X) denote the orthogonal galvanometer mirror pairs, which accounts to the y-axis scanning and x-axis scanning respectively. L1, L2, L3, L4: lens. ii) The image on the Fourier plane of the scan lens L1 after a slit is placed along the beam path. iii) The expected intensity distribution of the scanning laser beam on the Fourier plane of the scan lens L3 with the single line vertical galvanometer scanning. iv) The image on the Fourier plane of L3 with both galvanometer scanning mirrors active.

b) Experimental result of controlled photobleaching on a fluorescent pollen grain. i) Image of the pollen i) before and ii) after multi-site photobleaching. (Scale bar 10 μm) iii) Measured distance between two closest photobleached areas. The bleaching time for each area is 1 second.

Figure 3

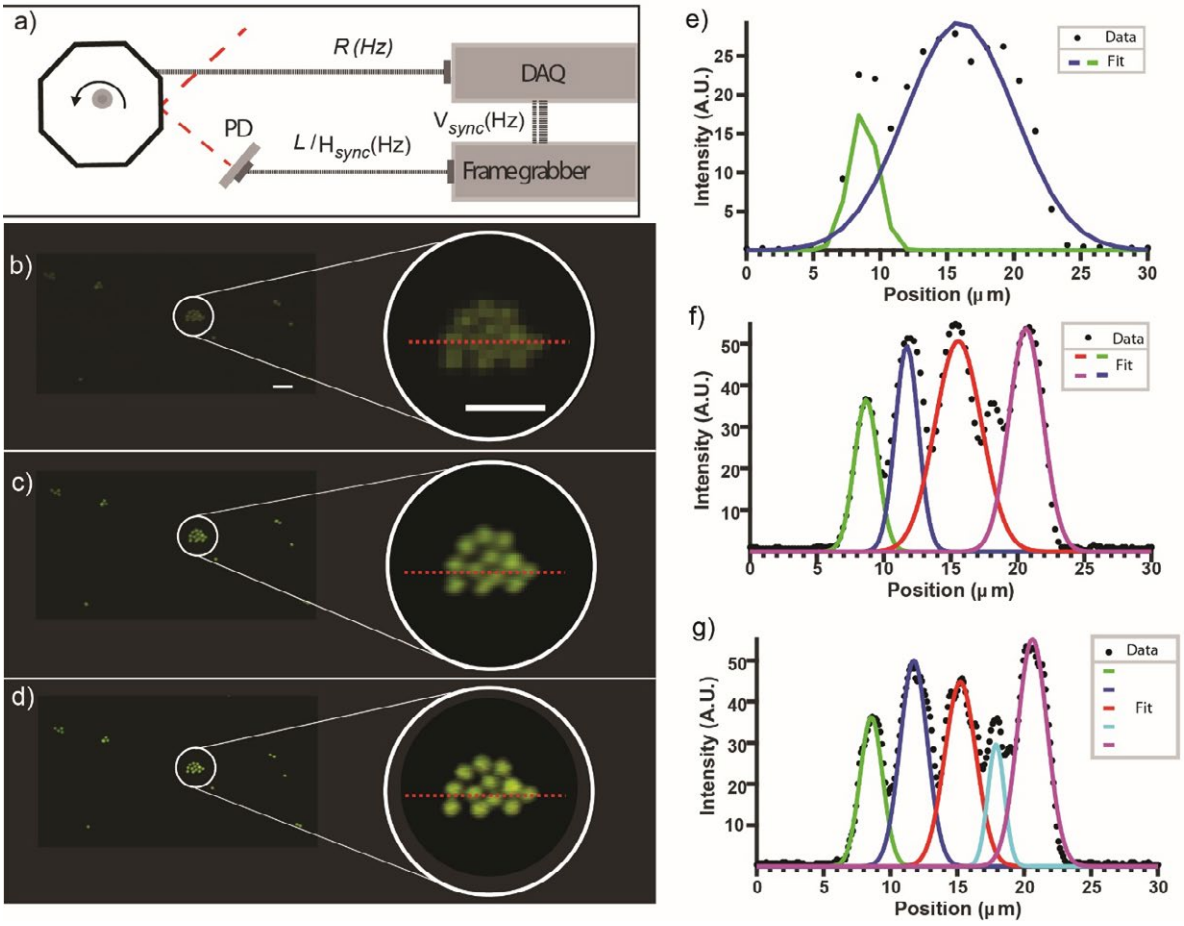

Figure 3: Oversampling for high pixel density

a) Schematic showing the interdependence of scanning rate and sampling rate necessary to achieve high resolution. Signal from the PD provides the Hsync signal L to frame grabber. Counter signal generated by PCI6110 (DAQ) provides the driving signal to control the speed to match the image format and frame rate. R is the reference frequency signal to control the rotation speed of polygon. b) Imaging of aggregate of 3 µm fluorescence beads (rainbow) captured with 512 x 512 pixels, with 20 fps at pixel size of 1.2 µm (line rate 10.8 kHz). c) and d) display same image area at same line rate of 10.8 kHz, but in c) there are 5-fold higher density of pixels than b). d) displays 10-fold increased pixel number but slower imaging speed of 10 fps (line rate 5.4 kHz). e), f) and g) shows the line plot and Gaussian fit of cross-section of the intensity across the red dashed line in images shown in b), c) and d) (Scale bar 20 µm).

Figure 4:

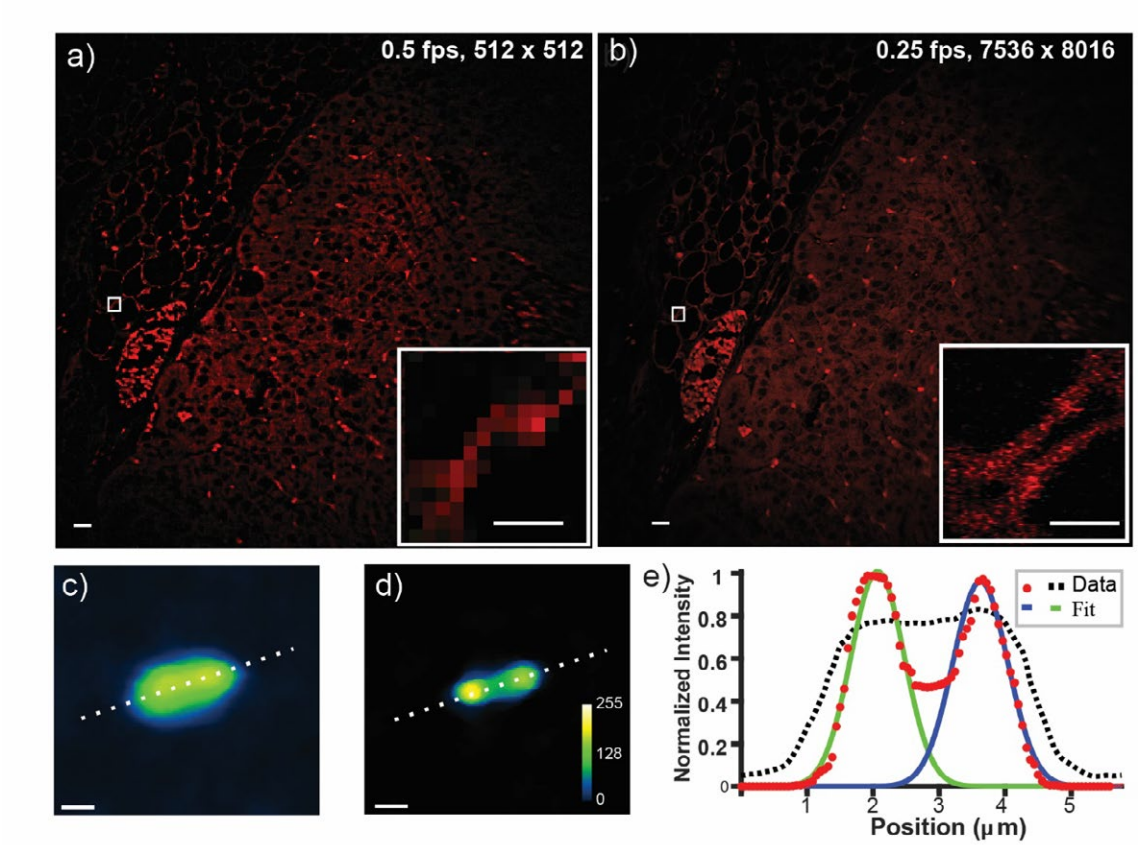

Figure 4: Wide field imaging histology sample of kidney slices
a) Average frame of 512 µm by 512 µm with 2 s averaged. b) Image captured with 20 x more pixels without averaging at 5 s (Scale bar 20 µm). Inserts show the digitally cropped image (Scale bar 5 µm). c) and d) show images of two closely packed 0.175 µm beads imaged with 10x pixel density before and after blind deconvolution respectively. e) shows a normalized intensity plot (white dotted lines in c) and d) to compare the resolution improvement. (Scale bar 1 µm).

Figure 5:

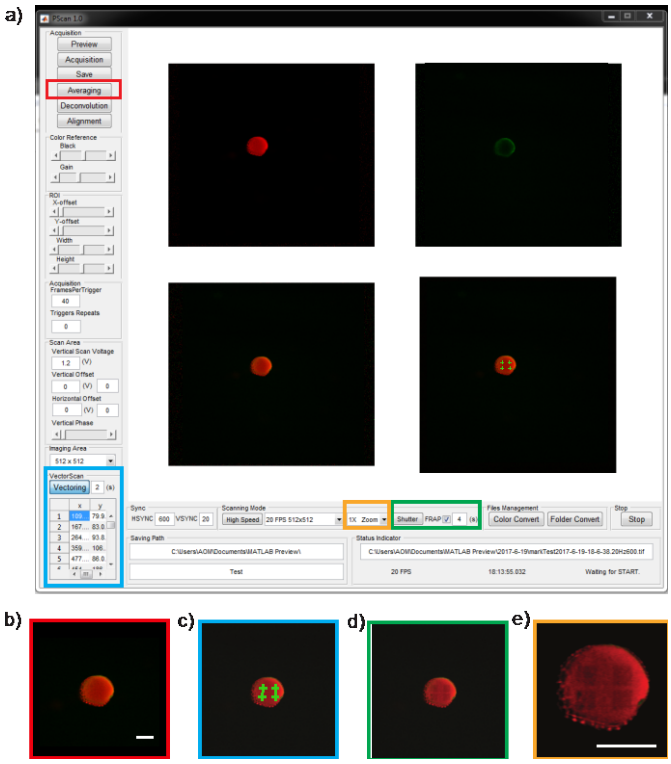

Figure 5: Automated localized photobleaching and oversampling using PScan 1.1

a) GUI of the customized software PScan 1.1 with improved functional controls for deconvolution, automated photomanipulation, digital magnification and imaging speed. b) Averaged image of a fluorescent pollen grain before modulation together with labelled target bleaching sites (denoted by green crosses) (Scale bar 20 µm). c) Each site can be chosen by either mouse control or direct input through the data table (green cursor). Additional dwelling time at each site can be selected d) Averaged image of the pollen after the bleaching (dwell time for each site was 0.5 s). e) Enlarged image upon photobleaching after increasing sampling ratio by 5-fold. (Scale bar 20 µm).

Figure 6

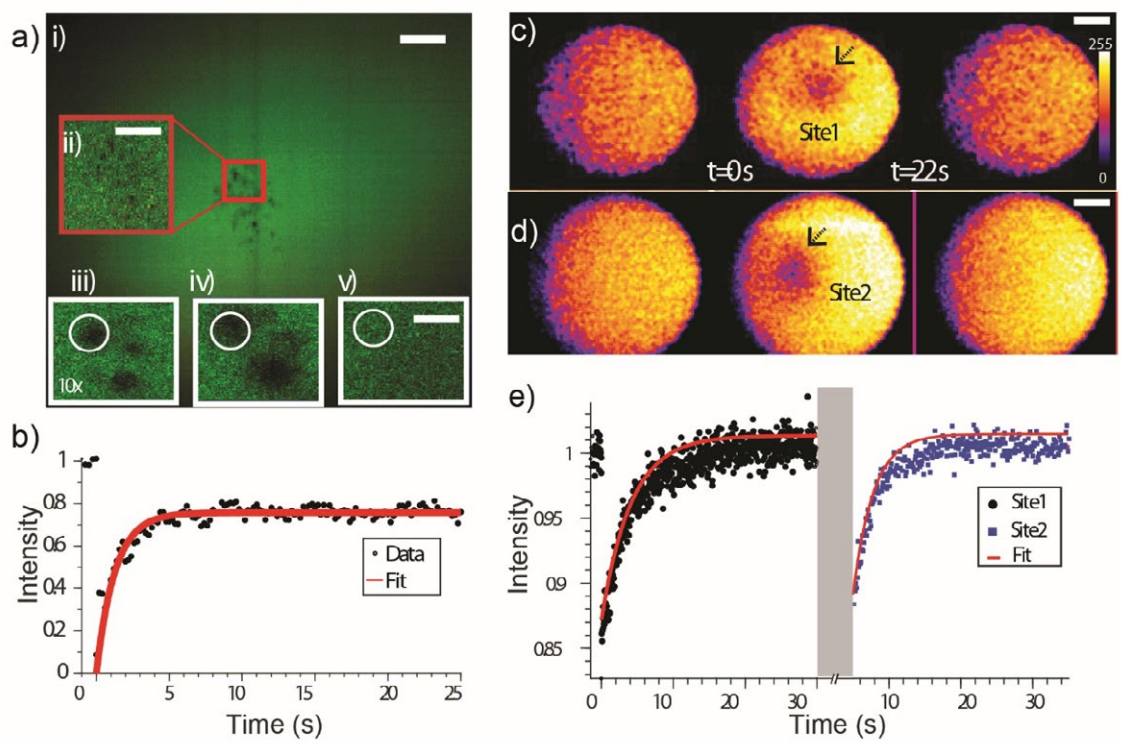

Figure 6: Controlled fluorescence after photobleaching (FRAP) on fluorescein and GUVs

a) time averaged image of a FITC solution directly after photobleaching with pixel size of 1.2 µm (Scale bar 10 µm). i) shows a cropped single frame without averaging image of a) at the photobleaching region of interest. ii) iii) iv) are photobleached sites taken sequentially from 1s to 22 s at pixel size of 120 nm at 10 x mode (Scale bar 1 µm). b) Line plot of fluorescence recovery over time. c) Image of fluorescence GUV over different time points; before and after photobleaching at pixel size of 200 nm. d) and e) Image of same GUV fluorescence at pixel size of 100 nm at different time points and different photobleaching site. f) Line plot of fluorescence recovery over time. (Scale bar 10 µm)

Figure 7

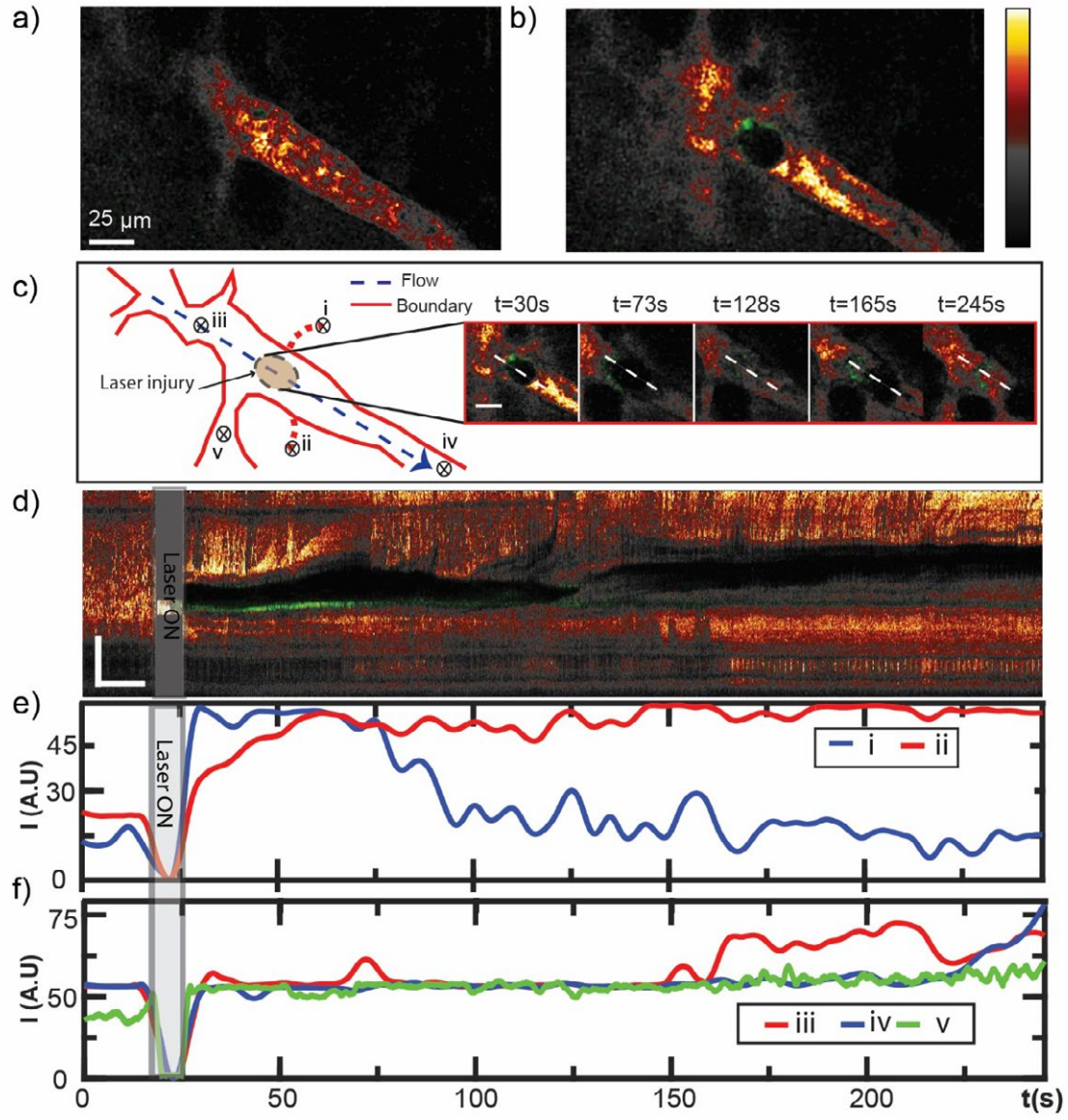

Figure 7: Imaging of a thrombus formed *in vivo* following laser injury to a blood vessel of a C57BL/6 wild-type mouse

Laser injury was induced by exposing the vessel wall to a localized high laser power illumination (180 mW) over 27 s. Thrombus formation was observed immediately following injury and images were captured continually. Fluorescence signal within the vasculature is from dextran rhodamine. Representative images show

a) A single frame with 0.24 μm pixel size captured by 20 fps over FOV of 226 μm x 123 μm.

b) Occlusion formed after laser exposure to a localized high laser power illumination: 180 mW for 27 s exposure time (two sequenced illumination, slit flipped into place for ablation with 18 s, followed by imaging for 20 s and slit switched on for a further 9 s). The vessel wall was damaged at the laser injury site resulting in leakage of blood from the vessel. Platelets accumulated and a thrombus was formed, causing occlusion of the blood vessel, thus the fluorescence intensity of the blood in the vessel is increased following laser injury with blood leaking and accumulation.

c) Schematic diagram of the imaged vessels, sites i) to v) are chosen areas where fluorescence intensity was measured temporally and plotted in e). i) and ii) are the two sites of injury with bleeding. iii) to v) are the sites inside the vessel. The insert diagrams are segmented images of the thrombus area at 30 s, 73 s, 128 s, 165 s and 245 s respectively. (Scale bar 25 μm).

At t=73 s, the blood leakage at injury site i is reduced, however the vessel wall appears to be expanded. The vessel is occluded and blood flow prevented and therefore increasing the signal intensity at the trunk.

After 128 s, the thrombus formed in the vessel embolized and blood flow is resumed to branch 1 with reduced fluorescence intensity in the vessel being observed.

d) The changes in the vessel diameter over time following laser injury. The image evaluates vessel diameter at the position indicated by the white dash line in c), with the width of the dark band (accumulated platelets) in the middle representing the thickness of the thrombus formed. (Scale bar 50 μm, 15 s).

e) Shows the temporal change in fluorescently labelled dextran signal intensity at the two injury sites (i) and (ii).

f) Depicts the signal intensity of three areas of blood flow at regions iii), iv) and v) within the vascular bed shown in c).

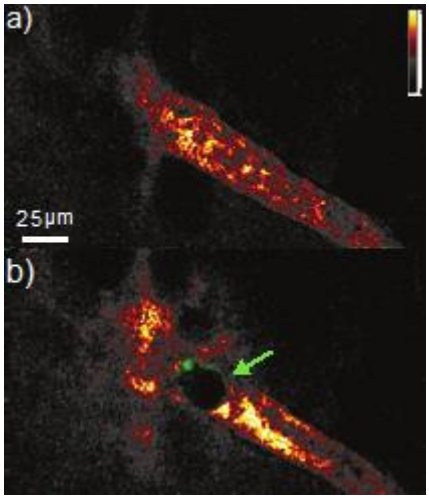

AbstractGraphical.jpg

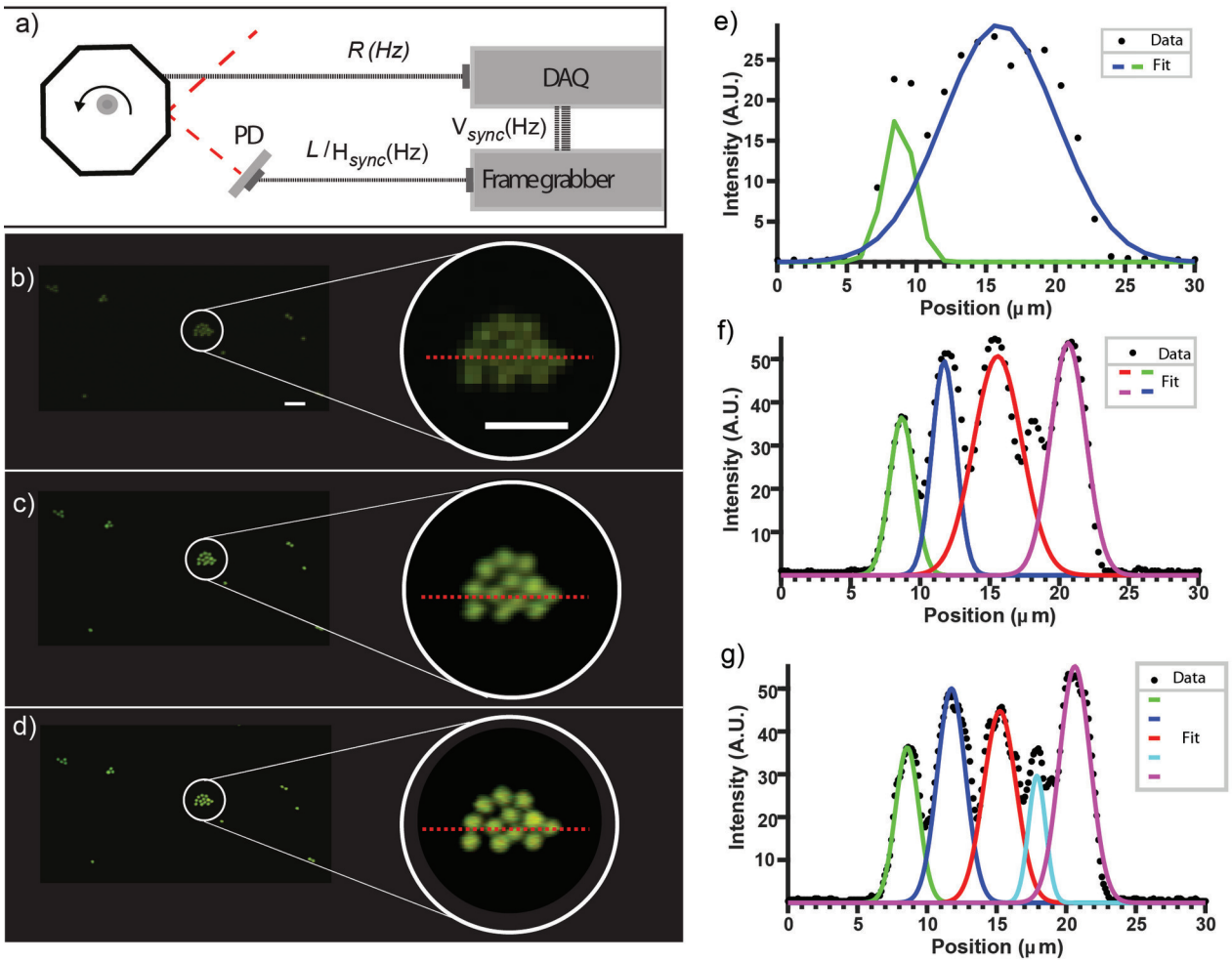

figure3_v4-01.jpg

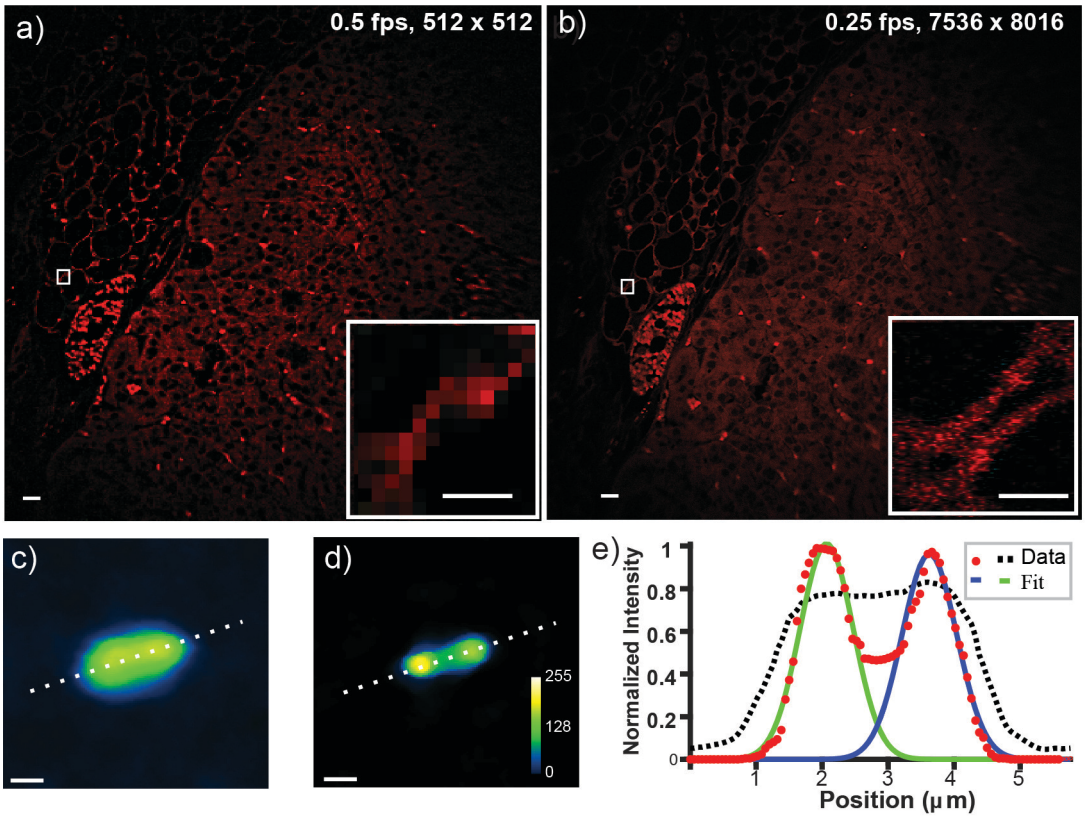

figure4_v7-01-01.jpg

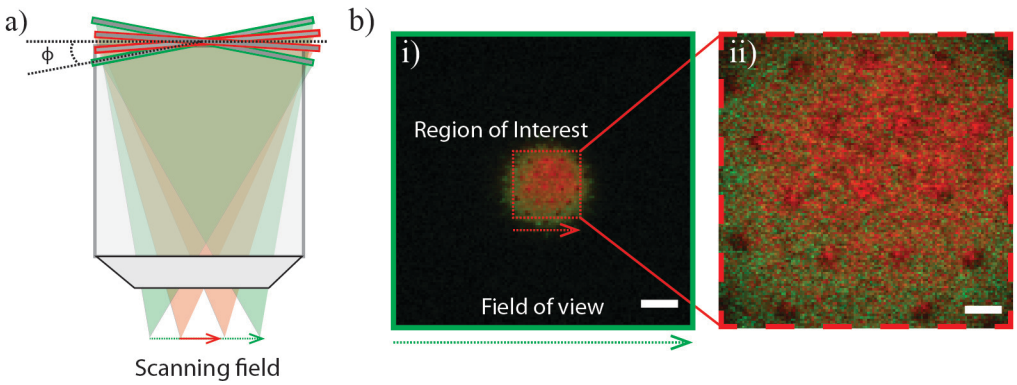

Figure1v1-01.jpg

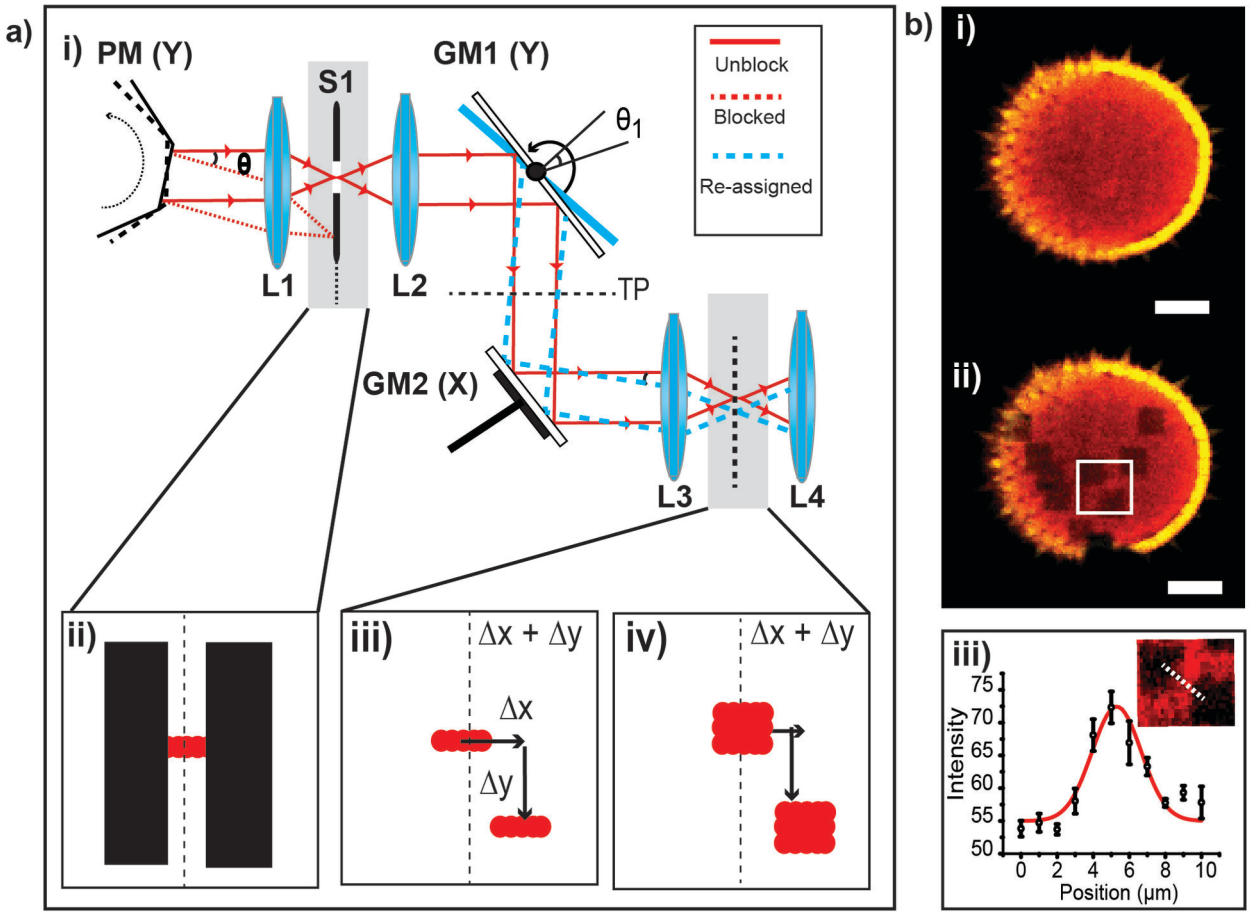

Figure2-01.jpg

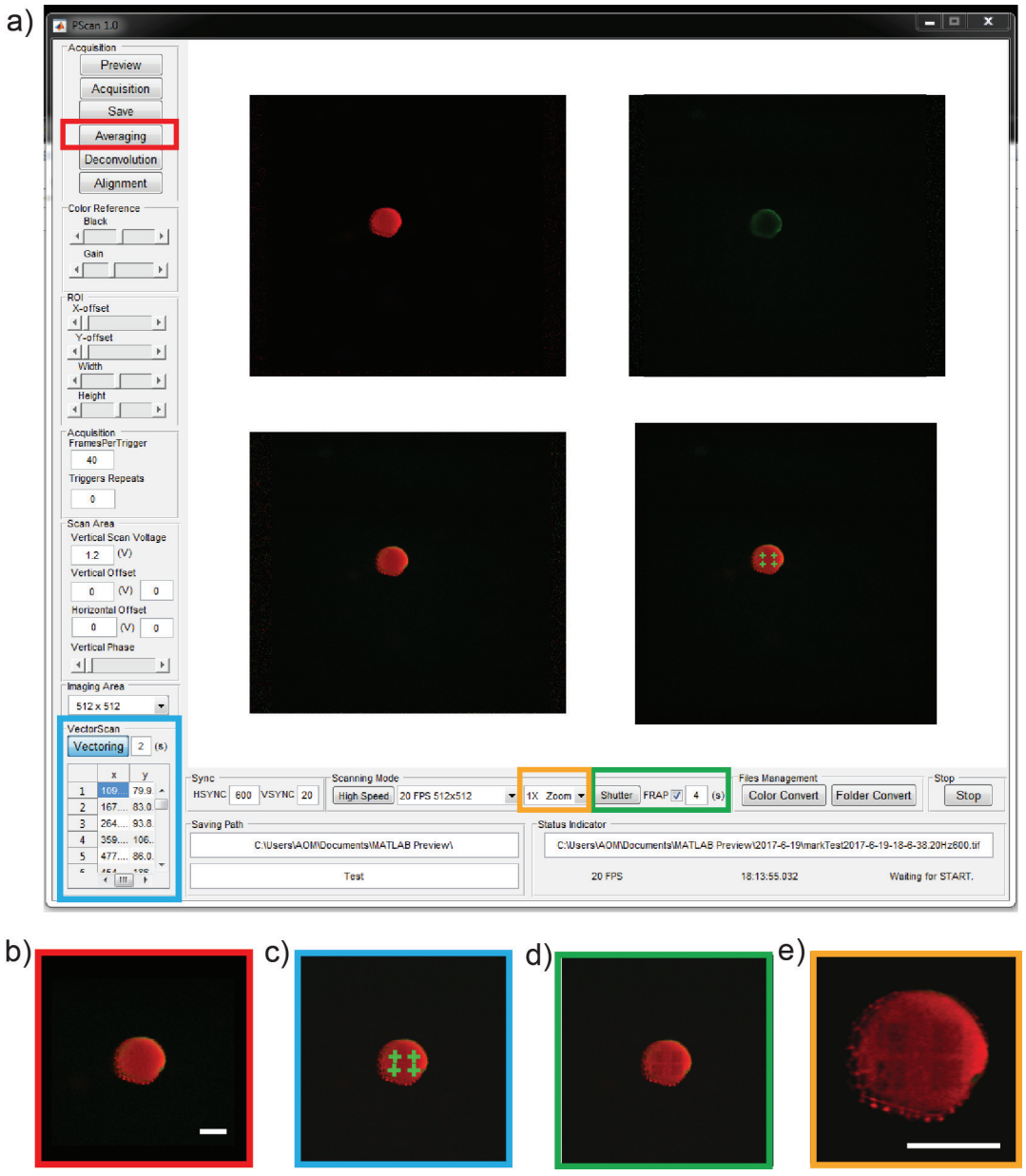

Figure5_v8-01.jpg

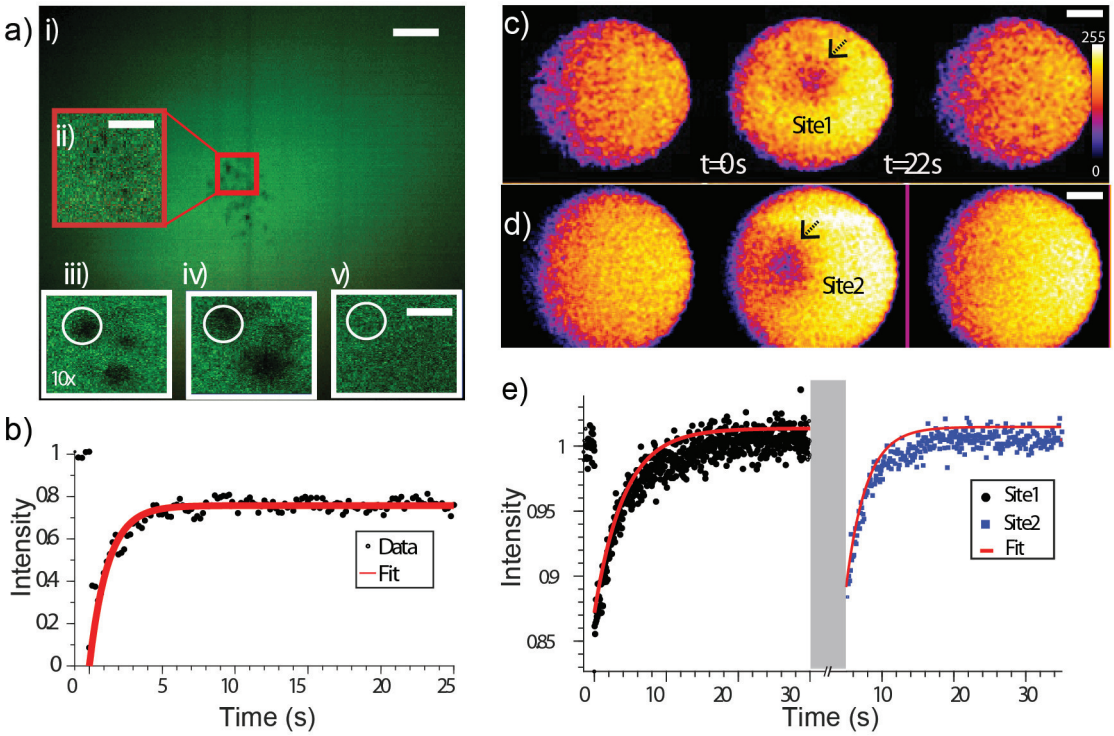

Figure6_v6-01.jpg

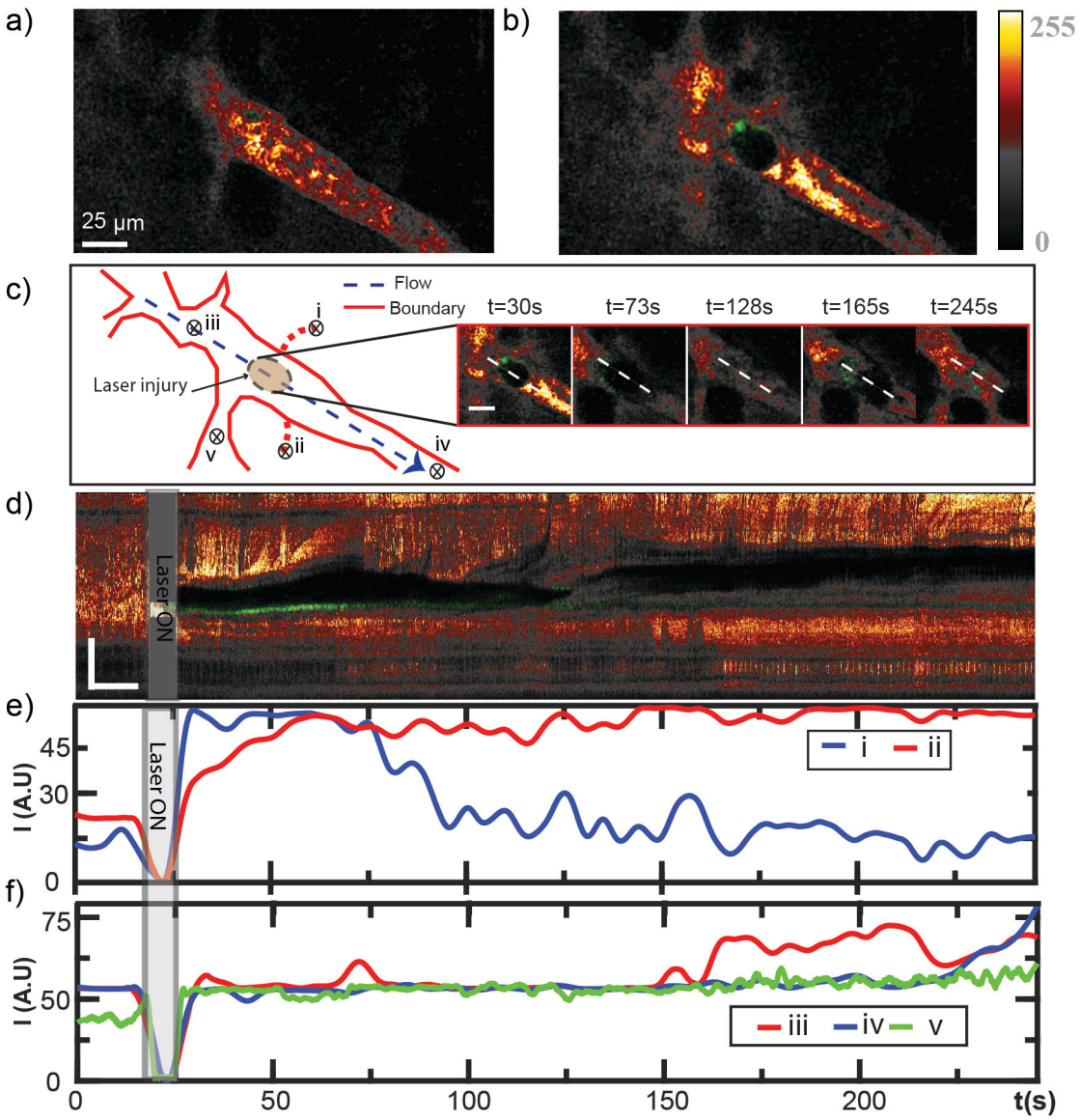

Figure7_v1-01.jpg